Supporting Information

Magnetic Enhancements of Defect-Mediated Spin Polarized Photocatalytic CO_2 Reduction of $Sn_2P_2S_6$

Chih-Ying Huang[1,2,†], Cheng-Yu Yu[3,†], Batjargal Sainbileg[4,†], Ying-Jun Chen[5], Cheng-Chieh Lin[1,2], Hsin-Lien Tsou[5], Ting-Rong Ko[4], Yung-Hung Huang[1,2], Michitoshi Hayashi[4], Ching-Hwa Ho[6], Heng-Liang Wu[1,4,*], Chia-Chun Chen[5,*], Chun-Wei Chen[1,3,4,*]

1. International Graduate Program of Molecular Science and Technology (NTU-MST), National Taiwan University, Taipei 10617, Taiwan
2. Molecular Science and Technology Program, Taiwan International Graduate Program (TIGP), Academia Sinica, Taipei 11529, Taiwan
3. Department of Materials Science and Engineering, National Taiwan University, Taipei 10617, Taiwan
4. Center for Condensed Matter Sciences, and Center of Atomic Initiative for New Materials (AI-MAT), National Taiwan University, Taipei 10617, Taiwan
5. Department of Chemistry, National Taiwan Normal University, Taipei, 11677, Taiwan
6. Graduate Institute of Applied Science and Technology, National Taiwan University of Science and Technology, Taipei, 106, Taiwan

† These authors contributed equally to this work.

Corresponding author: hengliangwu@ntu.edu.tw (H.-L. Wu), cjchen@ntnu.edu.tw (C.-C. Chen), chunwei@ntu.edu.tw (C.-W. Chen).

Synthesis of $Sn_2P_2S_6$ crystals

$Sn_2P_2S_6$ single crystals were synthesized by a chemical vapor transport (CVT) method. Elemental tin (Sn), phosphorus (P), and sulfur (S) powders were combined in a molar ratio of 1:1:3, together with iodine (10 mg cm^{-3}) as the transport agent, and sealed in an evacuated quartz ampoule (10^{-6} torr). The ampoule was subsequently placed in a horizontal three-zone tube furnace with a controlled temperature gradient. The source zone was heated to 600 °C and held to ensure complete compound formation, followed by increasing the growth zone temperature to 660 °C with a gradient of 2 °C cm^{-1} to facilitate vapor transport and recrystallization. The temperature profile was maintained for 360 h to allow sufficient crystal growth. During the process, iodine acted as the transport medium, enhancing sublimation of the source material and deposition in the growth zone. The obtained $Sn_2P_2S_6$ crystals displayed clean surfaces, layered morphology, and high structural quality, making them suitable for subsequent electronic and spectroscopic investigations.

Surface engineering of Vs-$Sn_2P_2S_6$

The as-prepared $Sn_2P_2S_6$ crystals were placed in a quartz boat and subjected to annealing in a tube furnace under an argon atmosphere. Prior to heating, the tube was purged with argon to establish an inert environment. The sample was annealed at 350 °C for 1 h to generate sulfur vacancies (Vs). Following the thermal treatment, the crystal color changed from light yellow to dark red, suggesting the formation of sulfur-deficient Vs-$Sn_2P_2S_6$. After cooling to room temperature under continuous argon flow, the obtained powders were collected and stored for subsequent structural characterization and photocatalytic evaluation.

Material characterizations

The morphology and crystallographic features of the samples were characterized by transmission electron microscopy (TEM, FEI Tecnai G2) together with selected-area electron diffraction (SAED). Surface morphology and elemental distribution were examined using field-emission scanning electron microscopy (FE-SEM, Hitachi S-4800) coupled with energy-dispersive X-ray spectroscopy (EDS). Phase composition and crystallinity were identified by X-ray diffraction (XRD, Bruker D8 Advance). Raman spectroscopy was performed using a custom-built micro-Raman system with a continuous-wave Nd:YAG laser (λ = 532 nm). Optical absorption properties were measured by ultraviolet–visible (UV-vis) spectroscopy using a double-beam PerkinElmer Lambda 365 spectrophotometer. Defect-related electronic

features were investigated by electron paramagnetic resonance (EPR, Bruker EPR-plus). Surface elemental composition and chemical states were analyzed by X-ray photoelectron spectroscopy (XPS, ULVAC-PHI) using monochromatic Al Kα and Cr Kα X-ray sources.

Photocatalytic CO_2 reduction

Photocatalytic CO_2 reduction experiments were carried out in a custom-designed aluminum reactor equipped with a quartz window to allow illumination by a solar simulator (Newport LSH-7320, Class ABA, AM 1.5 G, 100 mW cm^{-2}). Prior to each run, the reactor was cleaned, baked, and evacuated to remove residual gases, followed by purging with water vapor-saturated CO_2 (99.999%) for 30 min. A catalyst loading of ~2 mg was used for each experiment. For isotope-labeling studies, $^{13}CO_2$ (99 %, Cambridge Isotope Laboratories) was employed as the reactant gas. A schematic of the reaction setup is provided in Figure S1. Reaction products were collected using gastight syringes and analyzed by gas chromatography-mass spectrometry (GC-MS, Shimadzu GCMS-QP2020 NX) equipped with a Restek CP-PoraBOND Q column. The GC oven was programmed as follows: 25 °C for 1 min, ramp to 50 °C at 5 °C min^{-1}, then to 150 °C at 30 °C min^{-1}. Helium was used as the carrier gas at a flow rate of 1.8 mL min^{-1} with a split ratio of 1:10. The ion source temperature was set at 200 °C. Data acquisition and peak integration were performed using Shimadzu GC-MS solution software, and calibration curves for CO and CH_4 (Figure S2) were applied for quantitative analysis. For magnetic field-assisted experiments, permanent magnets of varying strength were positioned beneath the reactor, generating fields in the range of 0 to 300 mT (measured with a Gauss meter, PCE-MFM 3500-ICA).

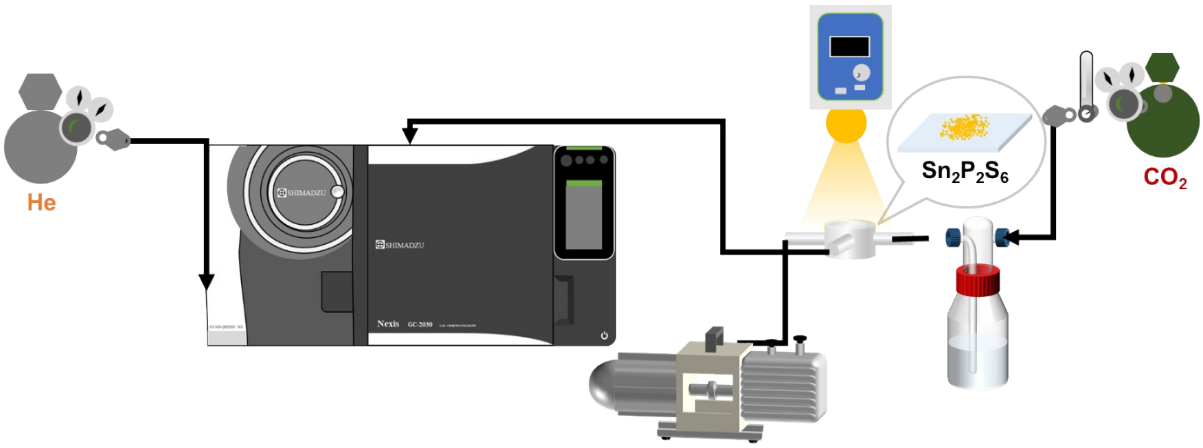

Figure S1. Schematic illustration of the custom-designed reactor system for photocatalytic CO_2 reduction under simulated solar irradiation, with controlled CO_2 flow, water vapor introduction, and product collection for GC-MS analysis.

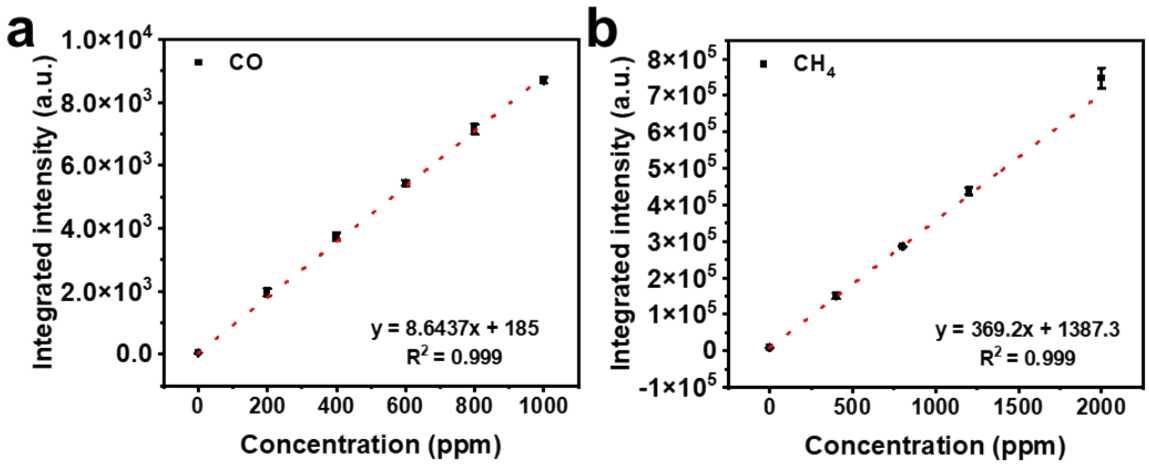

Figure S2. Calibration curves for (a) CO and (b) CH_4 obtained by GC-MS, used for quantitative analysis of photocatalytic products.

In situ DRIFTS analysis under magnetic field

In situ DRIFTS was performed on a Thermo Nicolet 6700 FTIR spectrometer equipped with a HgCdTe detector and a three-window DRIFTS cell. This setup was used to investigate the CO_2 adsorption and reduction behavior of $Sn_2P_2S_6$ and Vs-$Sn_2P_2S_6$. Prior to measurements, the catalysts were degassed at 298 K under vacuum to remove physisorbed species. About 4 mg of sample was homogeneously mixed with dry KBr (200 mg total, 2 wt.%). The composite was then loaded into the DRIFTS cell, which was purged with high-purity Ar for 1 h, followed by the introduction of moist CO_2 for another 1 h to ensure adsorption equilibrium. A permanent magnet (~300 mT) was placed beneath the DRIFTS cell to probe magnetic modulation. Continuous illumination was applied to simulate photocatalytic conditions, and spectra were collected for 240 min to enable in situ monitoring of photoinduced adsorption dynamics and spin-dependent interactions.

Calculation details

Spin-polarized first-principles calculations based on density functional theory (DFT) were conducted using the *Vienna ab initio simulation package* (VASP, version 5.4.4), within the framework of plane-wave basis set and projector augmented wave (PAW) methods.[1-2] The exchange-correlation functional was applied with the PBE+U+D3, an improved version of the standard Perdew-Burke-Ernzerhof (PBE) functional, incorporating Hubbard's plus U parameter (U = 4.0 eV) and Grimme's D3 van der Waals interaction corrections. The plane-

wave cutoff energy of 400 eV was used along with Monkhorst-Pack k-point sampling of 1 × 4 × 4 mesh. The slab surface was constructed from the bulk unit cell by adding the 15 Å vacuum space along [100] direction. The structure and all atomic positions are fully optimized until reached the convergence criteria of energy (10^{-5} eV) and residual force (10^{-3} eV/Å).

In principle, the formation of CH_4 requires eight electrons. For photocatalysts, CO_2 reduction and O_2 evolution simultaneously take place, as follows:

$$CO_2 + 8H^+ + 8e^- \rightarrow CH_4 + H_2O \quad (1)$$

$$H_2O + 2h^+ \rightarrow 1/2O_2 + 2H_2O \quad (2)$$

The possible reduction path is estimated by the Eq 3-10:

$$* + CO_2 + e^- + H^+ \rightarrow COOH^* \quad (3)$$

$$COOH^* + e^- + H^+ \rightarrow CO^* + H_2O \quad (4)$$

$$CO^* + e^- + H^+ \rightarrow CHO^* \text{ or } CO^* \rightarrow CO\uparrow + * \quad (5)$$

$$CHO^* + e^- + H^+ \rightarrow CH_2O^* \quad (6)$$

$$CH_2O^* + e^- + H^+ \rightarrow CH_3O^* \quad (7)$$

$$CH_3O^* + e^- + H^+ \rightarrow CH_4\uparrow + O^* \quad (8)$$

$$O^* + e^- + H^+ \rightarrow OH^* \quad (9)$$

$$OH^* + e^- + H^+ \rightarrow H_2O + * \quad (10)$$

where the asterisks (*) represent the active sites in the catalyst and the vertical arrows (↑) implies the release products.

Gibbs free energies were calculated at 298.15 K as follows,

$$G = E_{DFT} + E_{ZPE} - T \cdot S \quad (11)$$

where E_{DFT} , E_{ZPE} , and $T \cdot S$ are the electronic energy, the zero-point vibrational energy, as well the entropy contribution at the temperature of 298.15 K during the reaction process. Besides, the free energy change (ΔG) corresponds to subsequent reaction steps is expressed as:

$$\Delta G[COOH^*] = G[COOH^*] + 7 \times G[H^+ + e^-] - (G[*] + G[CO_2] + 8 \times G[H^+ + e^-]) \quad (12)$$

$$\Delta G[CO^*] = G[CO^*] + G[H_2O] + 6 \times G[H^+ + e^-] - (G[*] + G[CO_2] + 8 \times G[H^+ + e^-]) \quad (13)$$

$$\Delta G[CHO^*] = G[CHO^*] + G[H_2O] + 5 \times G[H^+ + e^-] - (G[*] + G[CO_2] + 8 \times G[H^+ + e^-]) \quad (14)$$

$$\Delta G[CH_2O^*] = G[CH_2O^*] + G[H_2O] + 4 \times G[H^+ + e^-] - (G[*] + G[CO_2] + 8 \times G[H^+ + e^-]) \quad (15)$$

$$\Delta G[CH_3O^*] = G[CH_3O^*] + G[H_2O] + 3 \times G[H^+ + e^-] - (G[*] + G[CO_2] + 8 \times G[H^+ + e^-]) \quad (16)$$

$$\Delta G[O^*] = G[O^*] + G[CH_4] + G[H_2O] + 2 \times G[H^+ + e^-] - (G[*] + G[CO_2] + 8 \times G[H^+ + e^-]) \quad (17)$$

$$\Delta G[OH^{*}] = G[OH^{*}] + G[CH_4] + G[H_2O] + G[H^{+} + e^{-}] - (G[*] + G[CO_2] + 8 \times G[H^{+} + e^{-}]) \quad (18)$$

$$\Delta G[*+ H_2O] = G[*] + G[CH_4] + 2 \times G[H_2O] - (G[*] + G[CO_2] + 8 \times G[H^{+} + e^{-}]) \quad (19)$$

Herein, the free energy of the proton-electron $(H^{+} + e^{-})$ pair is estimated by

$$G[H^{+} + e^{-}] = 1/2G[H_2] - eU \quad (20)$$

where U is the applied overpotential and e is the elementary charge ($U = 0\,V$ in this work).

$$\max[r.d.s] = [\max(\Delta E_{COOH}, \Delta E_{CHO}, \Delta E_{CH_2O}, \Delta E_{CH_3O}, \Delta E_{O}, \Delta E_{OH}, \Delta E_{*+ H_2O})] \quad (21)$$

where $max[r.d.s]$ is the maximum free energy difference (e.g. $\Delta E_{CHO} = \Delta G_{CHO} - \Delta G_{COOH}$) in the reaction, referred to as a rate determining step (r.d.s).

Supplementary Figures

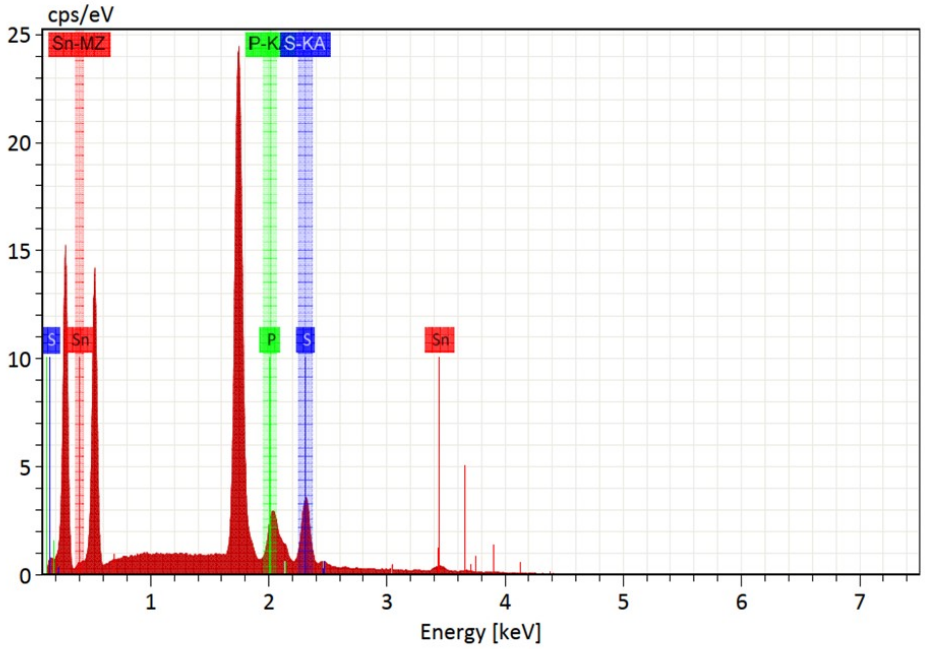

Element	At. No.	Line s.	Netto	Mass [%]	Mass Norm. [%]	Atom [%]	abs. error [%] (1 sigma)	abs. error [%] (2 sigma)	abs. error [%] (3 sigma)
Phosphorus	15	K-Serie	10342	5.79	17.09	27.28	0.31	0.62	0.92
Sulfur	16	K-Serie	14762	11.51	33.96	52.34	0.60	1.20	1.80
Tin	50	L-Serie	1982	16.59	48.95	20.38	1.56	3.13	4.69
			Sum	**33.90**	**100.00**	**100.00**			

Figure S3. EDS spectrum and quantitative analysis of $Sn_2P_2S_6$, confirming the presence of Sn, P, and S elements with an atomic ratio close to the stoichiometric composition.

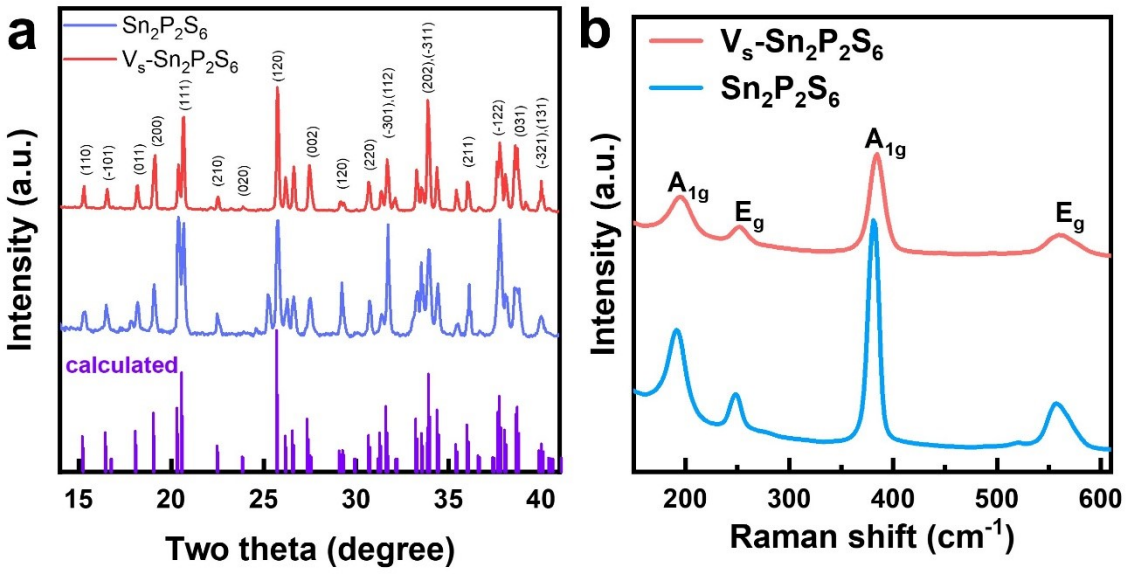

Figure S4. Structural characterizations of pristine $Sn_2P_2S_6$ and Vs-$Sn_2P_2S_6$. (a) XRD patterns confirming the monoclinic phase for both samples.[3] (b) Raman spectra showing characteristic vibrational modes and peak broadening upon sulfur-vacancy introduction.

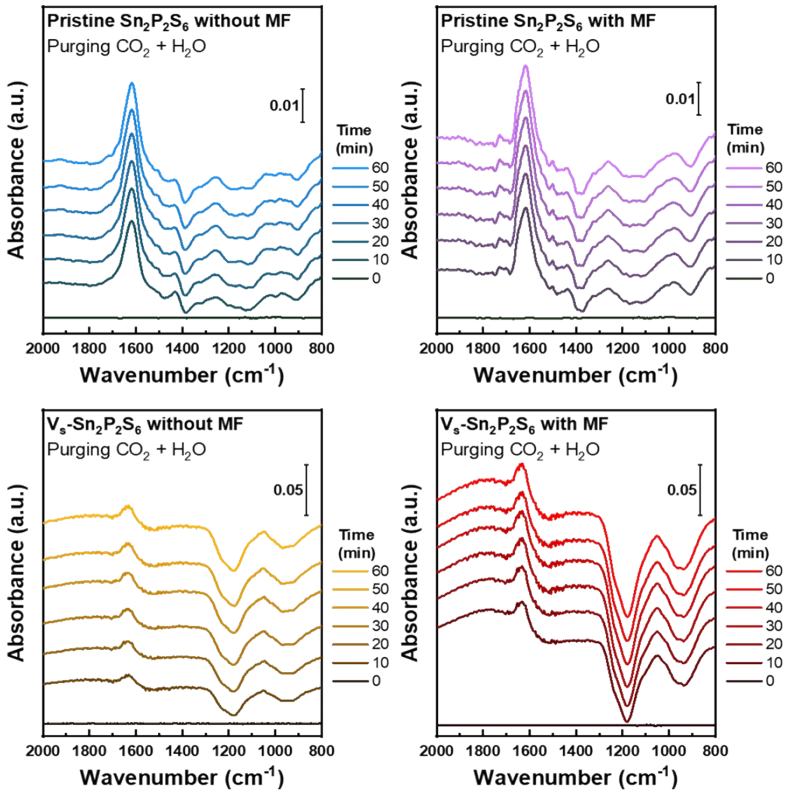

Figure S5. DRIFTS spectra of pristine $Sn_2P_2S_6$ and Vs-$Sn_2P_2S_6$ recorded after purging with CO_2 saturated with water vapor for 60 min. These spectra represent the background state before photocatalytic CO_2 reduction measurements.

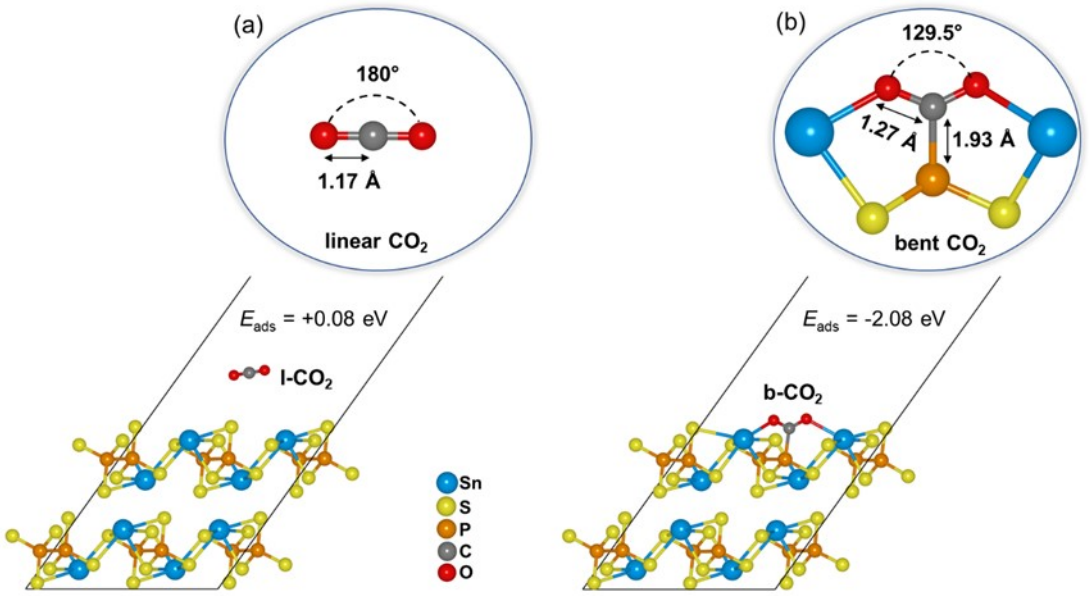

Figure S6. Optimized geometries of CO_2 adsorption on pristine $Sn_2P_2S_6$ and Vs-$Sn_2P_2S_6$. (a) On the pristine surface, the CO_2 molecule remains in a linear configuration (l-CO_2) with weak interaction. Since the CO_2 on the pristine surface is not absorbed with negligible E_{ads}, the subsequent reactions cannot proceed in the calculation. (b) On the Vs-$Sn_2P_2S_6$ surface, CO_2 binds at the vacancy site and adopts a bent configuration (b-CO_2), reflecting stronger interaction and facilitated activation.

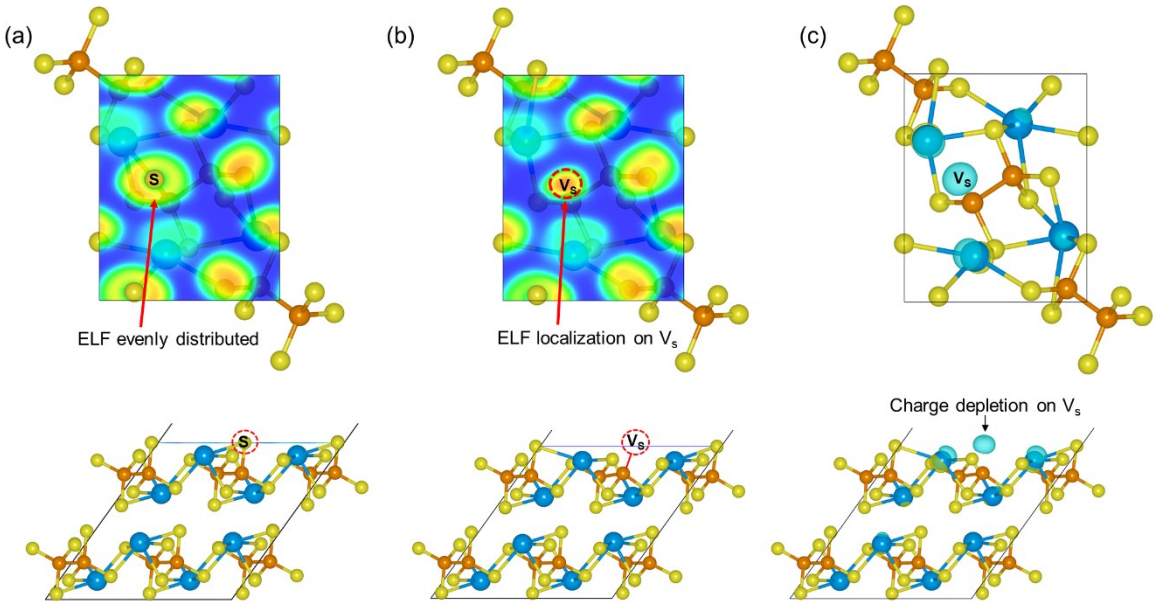

Figure S7. Electron localization function (ELF) analysis of pristine $Sn_2P_2S_6$ and Vs-$Sn_2P_2S_6$. (a) ELF profile of pristine $Sn_2P_2S_6$ showing delocalized charge distribution around the S site. (b) ELF profile of Vs-$Sn_2P_2S_6$ with enhanced localization at the vacancy site. (c) Charge density difference map of Vs-$Sn_2P_2S_6$ relative to pristine $Sn_2P_2S_6$, illustrating charge depletion at the sulfur vacancy site.

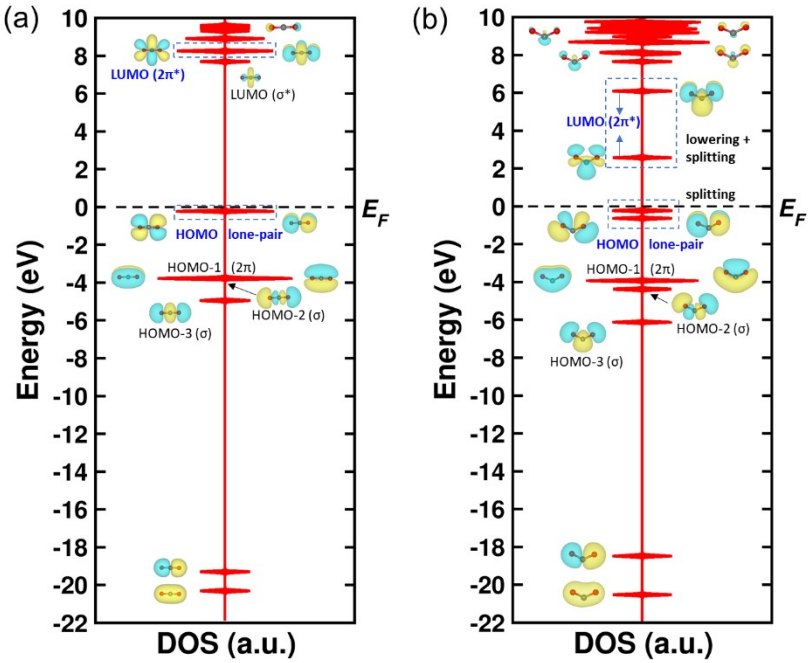

Figure S8. Density of States (DOS) of (a) l-CO_2 and (b) b-CO_2 with the corresponding molecular orbital (in the inset). LUMO (2π*) is significantly lowered and split, indicating the electron acceptance from Vs-$Sn_2P_2S_6$, whereas HOMO (lone-pair) is split, suggesting the electron donation to Vs-$Sn_2P_2S_6$.

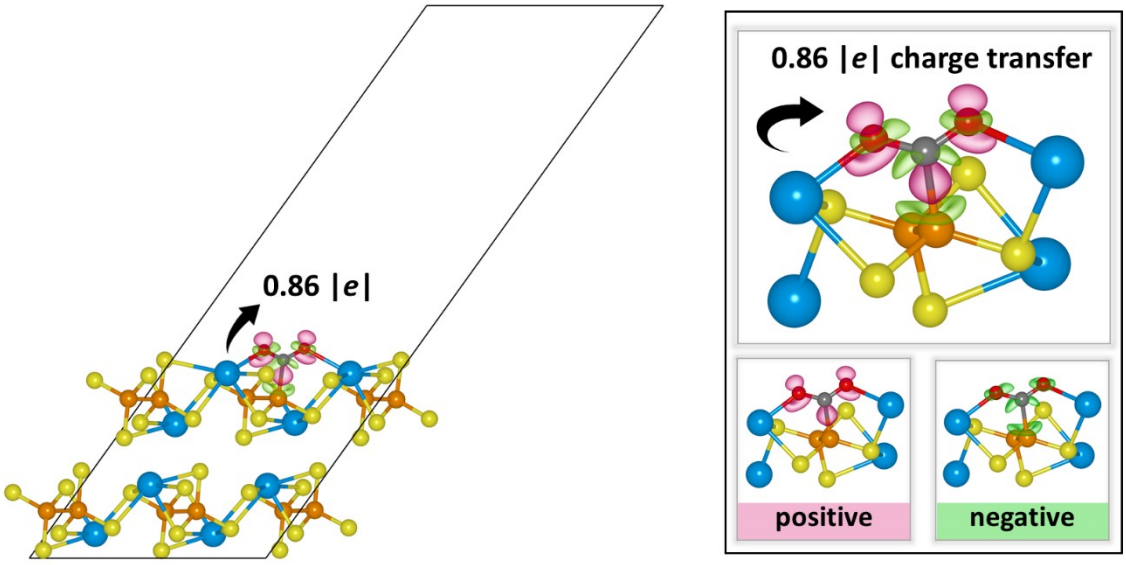

Figure S9. Bader charge and charge density difference (CDD) plots. The Vs-$Sn_2P_2S_6$ transfers a significant amount of charge to b-CO_2 through an acceptance-donation process. Red (green) isosurface represents the charge accumulation (depletion).

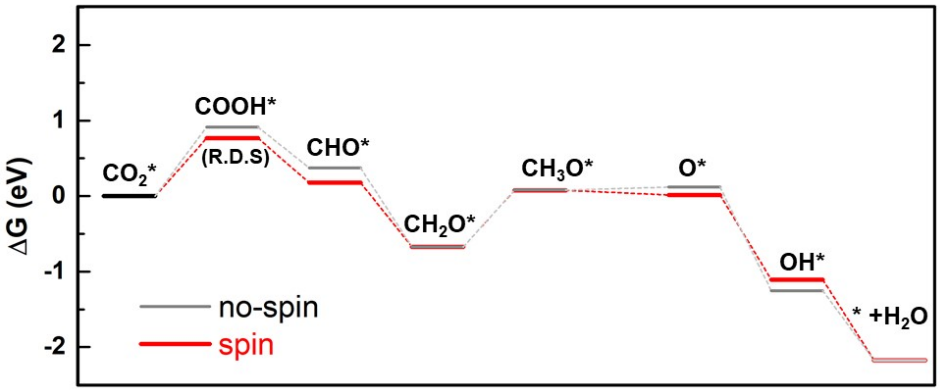

Figure S10. The Gibbs free energy diagram for the CO_2-to-CH_4 on V_S-$Sn_2P_2S_6$. Results from spin-polarized calculations are in red, while spin-unpolarized calculations are in grey. The spin-polarized calculation is energetically more favorable than the spin-unpolarized one.

Table S1. The free energy (G) of the adsorbed intermediates was calculated with thermal corrections at 298.15 K. The corresponding free-energy changes (ΔG) were then obtained according to the reaction equations (Eq. 12-19).

Intermediates	EDFT	EZPE	-TS	G	ΔG	ΔE
COOH*	-212.631	0.704	-0.188	-212.115	0.767	0.767#
CHO*	-205.718	0.543	-0.113	-205.288	0.178	-0.588
CH_2O*	-210.298	0.874	-0.117	-209.541	-0.672	-0.851
CH_3O*	-213.151	1.191	-0.234	-212.194	0.077	0.749
O*	-192.269	0.241	-0.189	-192.218	0.015	-0.062
OH*	-197.021	0.397	-0.118	-196.742	-1.106	-1.121
*+H_2O	-201.728	0.695	-0.178	-201.211	-2.173	-1.067

Note: The asterisk (*) represents the active site, while the hash (#) indicates a rate-determining step. The CO_2* is the first reference step, putting it at the zero. The energy difference (ΔE) between two reaction steps are estimated by the expression of $^{\Delta E_{CHO}} = \Delta G_{CHO} - \Delta G_{COOH}$.

Table S2. The calculated energy for gas (g) /liquid (l) phase and free energy corrections (eV).

Molecule	E_{DFT}	E_{ZPE}	-TS	G
CO_2 (g)	-22.98	0.36	-0.62	-23.24
H_2O (l)	-14.22	0.57	-0.571	-14.22
CH_4 (g)	-24.04	1.10	-0.50	-23.44
H_2 (g)	-6.76	0.20	-0.245	-6.805
1/2 H_2	-	-	-	-3.402

Reference

[1] Kresse, G., & Furthmüller, J. "Efficient iterative schemes for ab initio total-energy calculations using a plane-wave basis set", *Phys. Rev. B*, 1996, 54(16), 11169-11186.

[2] Perdew, J. P., Burke, K., & Ernzerhof, M. "Generalized gradient approximation made simple". *Phys. Rev. Lett.*, 1996, 77(18), 3865-3868.

[3] Haghighat-Shishavan, Safa, et al. "Realization of $Sn_2P_2S_6$-carbon nanotube anode with high K^+/Na^+ storage performance via rational interface manipulation–induced shuttle-effect inhibition and self-healing." *Chem. Eng. J.,* 2022, 435, 134965.